

Light charged particle production in the interaction of fast neutrons (25–65 MeV) with uranium nuclei

E. Raeymackers, S. Benck, I. Slypen, and J. P. Meulders

Institut de Physique Nucléaire, Université Catholique de Louvain, Chemin du Cyclotron 2, B-1348 Louvain-la-Neuve, Belgium

N. Nica and V. Corcalciuc

Institute of Atomic Physics, P.O. Box MG6, Heavy Ion department, Bucharest, Roumania

A. Koning

Nuclear Research and Consultancy Group NRG, P.O. Box 25, 1755 ZG Petten, The Netherlands

(Received 7 April 2003; published 25 August 2003)

Energy spectra (double-differential cross sections) for proton, deuteron, triton, and α -particle production in fast neutron induced reactions on uranium are reported for several incident neutron energies between 25 and 65 MeV. The spectra were obtained at nine laboratory angles between 20° and 160° and extrapolated and interpolated to other ten angles suitably covering the laboratory angular domain of 0° to 180° . The experimental setup and procedures for data reduction including corrections and normalization are presented and discussed. Based on the obtained double-differential cross sections, energy-differential and total cross sections are deduced as well. Theoretical calculations are based on GNASH and TALYS nuclear reaction codes which integrate the optical model, direct, preequilibrium, fission, and statistical nuclear reaction models in one calculation scheme.

DOI: 10.1103/PhysRevC.68.024604

PACS number(s): 25.40.Hs, 24.60.Gv, 28.20.-v

I. INTRODUCTION

Results of measurements on light charged particle (LCP) production for fast neutron induced reactions in the incident energy range of 20 to 80 MeV are rather scarce in the literature due to specific experimental difficulties. The present paper reports measurements of inclusive light charged particle emission spectra from natural uranium, at several incident neutron energies in the range of 25 to 65 MeV. The experiment was performed at the fast neutron facility of the Louvain-la-Neuve Cyclotron CYCLONE. The results on fast neutron induced light charged particle production on uranium shown here are the first reported in the literature in the 25 to 65 MeV incident neutron energy range.

In addition to the basic nuclear physics interest, the neutron induced reactions above 20 MeV are very important for the Accelerator Driven Systems (mainly transmutation of radioactive waste and alternative energy production) that are under development.

Inclusive energy spectra and their angular distributions (double-differential cross sections) for light charged particle (proton, deuteron, triton, and α -particle) emission from fast neutron reactions induced on uranium are reported at the following incident energies: 25.5 ± 1.5 , 28.5 ± 1.5 , 31.5 ± 1.5 , 34.5 ± 1.5 , 37.5 ± 1.5 , 41.0 ± 2.0 , 45.0 ± 2.0 , 49.0 ± 2.0 , 53.5 ± 2.5 , and 62.7 ± 2.0 MeV. The measurements were done at nine laboratory angles: 20° to 70° in steps of 10° and at 110° , 140° , and 160° .

In Sec. II, the experimental setup and the data reduction procedures, including normalization and corrections to the measured spectra, are discussed. Basic ingredients for the theoretical calculations are presented in Sec. III. The experimental results and comparison with theoretical calculations are shown in Sec. IV. Conclusions are given in Sec. V.

II. EXPERIMENTAL METHODS AND DATA ANALYSIS

The general layout of the fast neutron beam facility at the Louvain-la-Neuve Cyclotron (Fig. 1) has been described in detail in Refs. [1–3]. The 65 MeV accelerated proton beam is focused on a water-cooled 3 mm thick natural lithium target which produces a secondary beam of neutrons. With a proton beam current of 10^{-5} A, about 10^5 neutrons/cm²/s are available on the target situated in a first reaction chamber at 3.28 m downstream from the lithium target. The neutron energy spectrum at 0° consists of a well-defined peak located at 62.7 MeV of 2 MeV full width at half maximum (FWHM), which contains about 50% of all neutrons, followed by an approximately flat continuum of lower energy neutrons [3]. In the main peak there are about 10 times more neutrons/MeV than in the neutron lower energy continuum.

The first reaction chamber (503 mm in diameter) has nine different ports to accommodate the holding system of the telescopes. Six charged particle telescopes were used simultaneously during the experiment. Each of them consists of (i) a ΔE -type detector (NE102 plastic scintillator, 0.1-mm thick, 4 cm in diameter) viewed by a XP2020 photomultiplier via a lucite light guide, and (ii) an E-type detector [CsI(Tl) crystal, 22-mm thick, 38.1 mm in diameter], connected to a XP2262B photomultiplier. The E detector stops the protons with energy up to 80 MeV. A time-coincidence condition imposed between the ΔE and E detectors leads to the suppression of an important part of the otherwise high counting rate background produced in the experiment.

A natural uranium target of 6×6 cm² surface and 0.18 mm thick was used for the measurements. The angle of the target surface relative to the beam direction was chosen in order to minimize the path of the produced light particles in their travel to the detectors.

The protons and deuterons recoiling from respectively

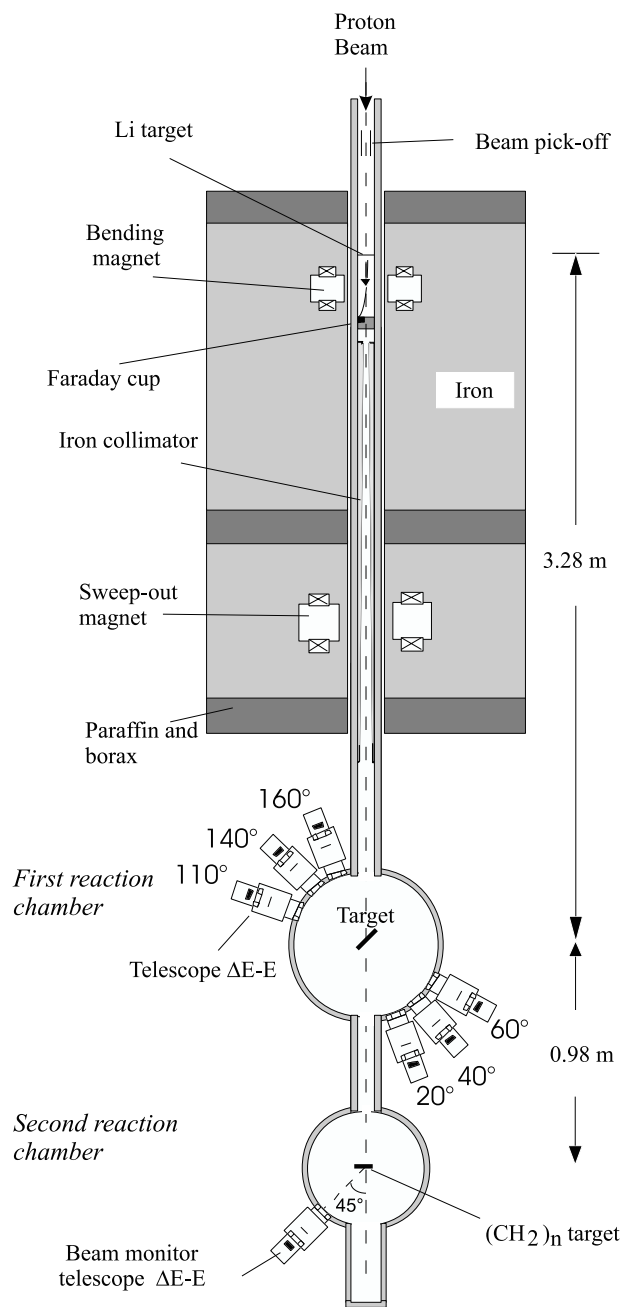


FIG. 1. General layout of the fast neutron facility at the Louvain-la-Neuve Cyclotron (not at scale).

1.0 mm thick polypropylene and 0.6 mm thick deuterated polypropylene targets were used for energy calibration. They were recorded at laboratory angles from 20° to 70° in steps of 10° , for each of the six telescopes. The $H(n,p)$ scattering is registered with good statistics, for a precise determination of differential cross sections to be subsequently used as a reference. An extra calibration point was obtained with a 5.5 MeV α -source. The set of calibration points thus obtained was used together with a three-parameter formula [3–5] in a simultaneous fit to provide the calibration curves for all four types of light charged particles measured in the experiment. This formula relates the CsI light response to the energy of each type of detected particle, allowing a reliable energy

calibration for tritons and α -particles as well.

For charged particle discrimination, a twofold separation procedure was applied: (i) by using the energy information from ΔE -E telescopes and (ii) by two different charge integration of the CsI signal [3,5,6]. In the latter case, the signal was integrated during a fast gate (600 ns wide) and a slow gate (2700 ns wide). A combined use of the two procedures [3] allows a reliable low energy background elimination and a good separation of the reaction products over their entire energy range. Figure 2 presents a particle separation spectrum in slow vs fast component representation, taken at 20° , before (a) and after (b) the elimination of the background.

Two beam monitoring systems (Fig. 1) were used. Behind the lithium target, the incident proton beam was deflected by a magnetic dipole and integrated into a water cooled Faraday cup. Downstream from the first reaction chamber and coupled to it, there is a second reaction chamber (Fig. 1) in which a 1.0 mm thick polypropylene target was placed. A charged particle telescope (2 mm thick NE102 scintillator as ΔE detector and a CsI(Tl) crystal as E detector) registered the $H(n,p)$ scattered protons at 45° laboratory. The total charge in the Faraday cup and the integral of the recoil proton peak served as beam monitors during the measurement [3]. The two monitoring systems were in very good agreement (less than 2% differences) during the experiment.

A total time of flight (TOF) between a capacitive beam pick-off located upstream from the neutron producing target (Fig. 1) and the ΔE detector is measured for each charged particle event in a telescope. Knowing the energy of the charged particle (from the energy calibration) and its flight path (distance from the target to the ΔE detector), one calculates the time of flight for each charged particle event which, when subtracted from TOF, gives the neutron time of flight, hence the energy of the corresponding incident neutron [3,7–9]. In this way, the incident neutron energy spectrum corresponding to each particle type is reconstructed at each detection angle. In Fig. 3 the inset presents an incident neutron energy spectrum reconstructed from all the proton events recorded at 20° laboratory with the uranium target. Based on the time resolution in the experiment (0.8 ns), a selection of only those charged particles induced by a specific incident neutron energy bin is performed. As an example, Fig. 3 illustrates the selection of the proton events induced by respectively the neutrons of the main peak (hatched area) and the neutrons of 41.0 ± 2.0 MeV energy (double hatched area). The statistics in the experiment corresponds to a total acquisition time of about 97 h for the forward angles and 185 h for the backward angles, with about 12×10^{-6} A mean proton beam on the lithium target.

The absolute normalization of the measured spectra is done relative to $H(n,p)$ scattering cross sections [10]. With each of the six telescopes, angular distributions for the n - p scattering were measured during the experiment at six laboratory angles between 20° and 70° . Therefore, for each telescope, six normalization points are determined, and the normalization factor is taken as their mean value. Generally, the spread of these values around the mean was less than 2%. Normalization factors of the order 2.5×10^{-3} mb/MeV/sr are obtained for charged particle events induced by neutrons

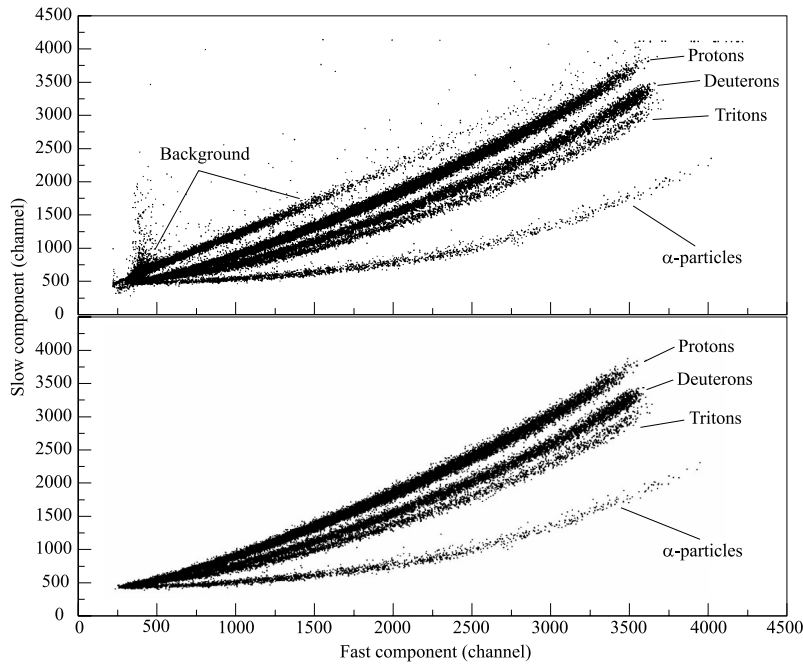


FIG. 2. Light charged particle discrimination spectrum measured by the telescope at 20° laboratory angle. Display of slow vs fast component of the CsI signal before (a) and after (b) the low energy background elimination.

in the main peak for the forward angles (and about half this value for the backward angles). Considering ten counts in an ejectile energy bin of 2 MeV, this corresponds to about 10^{-2} mb/MeV/sr indicating an inferior detection limit of the measurement, with an associated 33% statistical uncertainty. For data obtained at incident neutron energies from the flat continuum of the incident neutron energy spectrum, this limit becomes about ten times higher, due to the fact that there are about 10 times less neutrons in a low incident neutron energy bin than in the main peak.

The thickness of the target and of the ΔE detector and the threshold of the E detector limit the detection of the low energy charged particles. Only fractions of the entire target thickness towards the detector produce particles with enough energy to be detected. A Monte Carlo simulation program of the experiment [11] calculates the solid angles and thick tar-

get corrections. The program includes energy losses in the target material and in the ΔE detector, threshold of the E detector (about 1.5 MeV), reaction kinematics, neutron beam energy width, neutron beam profile, target-detector geometry, and the geometry of the collimation system of the detectors. The collimation of each charged particle telescope corresponds to an angular opening of $2^\circ - 3^\circ$. The calculated thick target correction factors for each of the charged particle products are mean values over the energy spread introduced by the target material and the ΔE detector.

The detection energy thresholds in the experiment were mainly given by the thickness of the ΔE detector and correspond to about 6 MeV for hydrogenlike ejectiles and 12 MeV for α -particles. The respective values of the Coulomb barriers are about 15 and 28 MeV for the uranium nucleus.

The reported cross sections for the α -particle include the

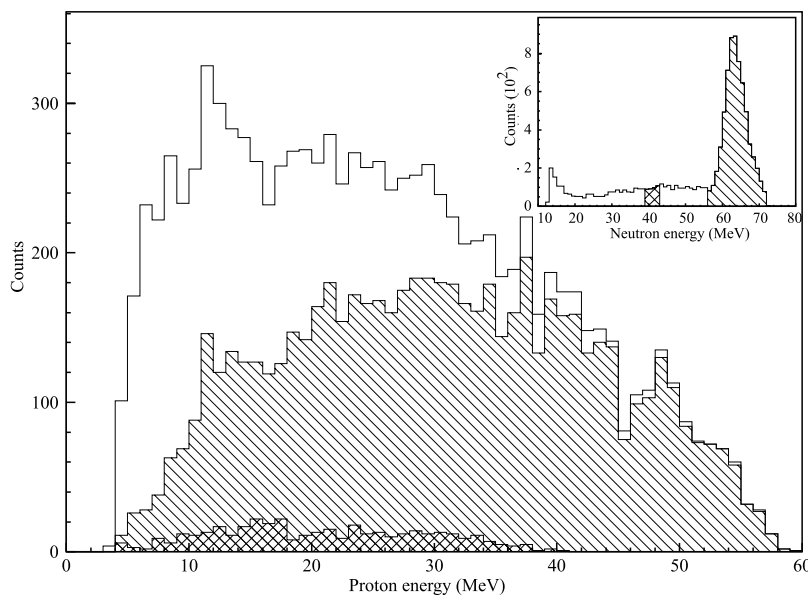


FIG. 3. All proton events (white histogram) and selection of proton events induced by the incident neutron energies of the 62.7 MeV main peak (hatched area) and of the 41.0 ± 2.0 MeV bin from the continuum (double hatched area). The inset shows the incident neutron energy spectrum reconstructed from all proton events at 20° .

^3He events that could not be separated from the α -particle events (Fig. 2). Nevertheless, their contribution is much smaller than that of the α -particles, being within the experimental errors. This conclusion is also supported by the theoretical calculations. A detailed description and discussion about the procedures used for data reduction is given in Refs. [3,7–11].

III. THEORETICAL BASIS

It has become customary to compare experimental data of the type presented in this paper to intranuclear cascade models or to calculations based on exciton models. In this latter case, taking into account the complexity and number of the open channels, a computational scheme is invoked which consists of direct plus preequilibrium reaction calculation followed by the subsequent compound nucleus decay of all possible residual nuclides by means of the Hauser-Feshbach statistical model. Basically the intranuclear cascade models are supposed to work at higher incident energies than the ones this paper is concerned with. In the comparison of the present experimental data, theoretical results obtained with two nuclear reaction codes GNASH [12] and TALYS [13] were used. While GNASH was widely applied in the last years, TALYS is a new code under development. Both codes integrate the optical model, direct, preequilibrium, fission and statistical nuclear reaction models in one calculation scheme and thereby give a prediction for all the open reaction channels. The purpose is to simulate nuclear reactions that involve neutrons, photons, protons, deuterons, tritons, ^3He , and α -particles in the 1 KeV–200 MeV energy range. Predicted quantities include integrated, single-, and double-differential cross sections, for the continuum and discrete states, residual production and fission cross sections, γ -ray production cross sections, etc. In this work, total, single- and double-differential cross sections are of interest.

The compound nucleus decay using Hauser-Feshbach statistical approach requires the determination of the transmission coefficients for particle emissions, from zero to the maximum of the emitted particle energy. The calculations begin with the extension of the optical potentials in order to describe the scattering of the various particles involved (neutrons and the four types of charged particles studied here) over a large energy range.

For the GNASH calculations, data on total and differential elastic, nonelastic, and total cross sections were compiled for heavy nuclei [14]. These data were compared to the optical model calculations performed with the spherical optical model code SCAT2 [15]. For protons and neutrons, the optical model parameters for lead [16] were modified by adjustment to the uranium experimental data. The transmission coefficients were obtained from the potential of Bojowald *et al.* [17] for deuterons, from the potential of Becchetti-Greenless [18] for tritons, and from the potential of McFadden [19] for the α -particles.

For the TALYS calculations, dedicated optical model potentials were developed for both neutrons and protons up to 200 MeV. The used parameters were mainly derived from the global optical model parameters [20]. These potentials pro-

vide the necessary reaction cross sections and transmission coefficients for the statistical model calculations. The ground-state rotational band states $0^+—2^+—4^+$, were included as collective coupled channels. More extensive coupling-schemes (including various vibrational bands) exist for uranium, but these are not expected to be of importance for the smooth high-energy continuum spectra that we analyze here. Collective transitions to the continuum were taken into account by contributions from the giant quadrupole and the low-energy and high-energy octupole resonances, whose deformation parameters were determined from the respective energy weighted sum rules. This effect, however, only shows up in the neutron channel and has a minor effect (only in terms of reducing the overall flux) in the charged-particle channels. For the outgoing proton channel, the proton global optical model parameters were used [20]. For complex particles, the optical potentials were directly derived from the nucleon potentials using Watanabe's folding approach [21].

Since the Coulomb barrier strongly inhibits compound nucleus evaporation, differences in transmission coefficients arising from different optical models have almost no effect for the reactions studied here. The only optical model related difference might come from the inverse reaction cross sections that enter the expression for the ejectile cross section in the exciton model and the neutron reaction cross section at the incident energy, which acts as an overall scaling factor in the particle-hole state density.

Preequilibrium emission takes place after the first stage of the reaction but long before statistical equilibrium of the compound nucleus is attained. It is imagined that the incident particle step-by-step creates more complex states in the compound system and gradually loses its memory of the initial energy and direction. In the exciton model [22,23], at any moment during the reaction, the nuclear state is characterized by the total energy and the total number of particles above and holes below the Fermi surface. Particles (p) and holes (h) are indiscriminately referred to as excitons. Furthermore, it is assumed that all possible ways of sharing the excitation energy between different particle-hole configurations with the same exciton number $n=p+h$ have equal *a priori* probability. To keep track of the evolution of the scattering process, one merely traces the temporal development of the exciton number, which changes in time as a result of intranuclear two-body collisions. The basic starting point of the exciton model is a time-dependent master equation, which describes the probability of transitions to more and less complex particle-hole states as well as transitions to the continuum (emission). Upon integration over time, the energy-averaged emission spectrum is obtained. These assumptions make the exciton model amenable for practical calculations. The price to be paid, however, is the introduction of a free parameter, namely, the average matrix element of the residual two-body interaction, occurring in the transition rates between two exciton states.

The exciton model that is used for the (nucleon, nucleon) reactions differs between GNASH and TALYS codes. The model implemented in GNASH is a one-component exciton model developed by Kalbach [24], with a parametrization for the energy dependence of the squared internal transition ma-

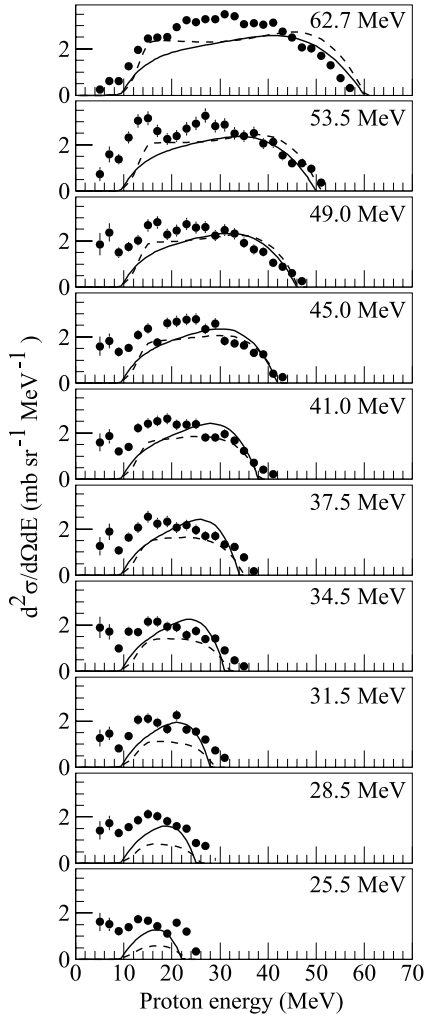


FIG. 4. Double-differential cross sections ($d^2\sigma/d\Omega dE$) for (n,px) reactions at 20° laboratory angle, for the indicated ten incident neutron energies (filled dots, in bins of 2 MeV). GNASH (dashed lines) and TALYS (continuous lines) code calculations are shown.

trix element M^2 , that has been validated at relatively low incident energies (below 40 MeV). There are indications that at higher incident energies, this energy dependence is no longer appropriate. This is indeed confirmed by the TALYS calculations, for which an M^2 value is used which, for 63 MeV incident energy, is twice that of the GNASH calculation, resulting in a somewhat softer spectrum at the highest incident energies, see Fig. 4. This result is not surprising—so far, matrix element parametrizations have been used that depend on energy through $E^{-1/2}$ or E^{-3} [24,25], which is basically equivalent to stating that at high incident energies there is no intranuclear scattering to more complex stages. It is more likely that matrix element will flatten, and maybe tend to a constant value, as a function of energy [26]. The exact form for this energy dependence is however still unknown. The numerical value of M^2 is not the only difference between the used methods. The default preequilibrium model of TALYS is the two-component exciton model of Kalbach [25]. In the two-component model, the neutron and proton type of the created particles and holes is explicitly followed throughout the reaction.

Following Ref. [25], the exciton model cross section is given as

$$\frac{d\sigma_k^{\text{EM}}}{dE_k} = \sigma^{\text{CF}} \sum_{p_\pi=p_\pi^0}^{p_\pi^{\text{eq}}} \sum_{p_\nu=p_\nu^0}^{p_\nu^{\text{eq}}} \omega_k(p_\pi, h_\pi, p_\nu, h_\nu, E_k) \times S_{\text{pre}}(p_\pi, h_\pi, p_\nu, h_\nu), \quad (1)$$

where $p_\pi(p_\nu)$ is the proton (neutron) particle number and $h_\pi(h_\nu)$ the proton (neutron) hole number. The initial proton and neutron particle numbers are $p_\pi^0=Z_p$ and $p_\nu^0=N_p$, with $Z_p(N_p)$ the proton (neutron) number of the projectile. Generally, $h_\pi=p_\pi-p_\pi^0$ and $h_\nu=p_\nu-p_\nu^0$ so that the initial hole numbers are zero, i.e., $h_\pi^0=h_\nu^0=0$ for primary preequilibrium emission. We adopt $p_\pi^{\text{eq}}=p_\nu^{\text{eq}}=6$, implying that the

TABLE I. Experimental and theoretical total production cross sections of this work for the four LCP types. The theoretical values for ^3He production are given in parentheses in the α -particle column.

E_n (MeV)	$\sigma(n,px)$ (mb)		$\sigma(n,dx)$ (mb)		$\sigma(n,tx)$ (mb)		$\sigma(n,\alpha x)$ (mb)	
	Exp.	TALYS	Exp.	TALYS	Exp.	TALYS	Exp.	TALYS
62.7 ± 2.0	367 ± 27	346.9	92 ± 11	66.2	41 ± 6	29.3	72 ± 16	33.7 (2.5)
53.5 ± 2.5	329 ± 68	270.8	105 ± 37	48.5	44 ± 17	23.6	54 ± 29	25.1 (1.1)
49.0 ± 2.0	271 ± 56	243.8	70 ± 25	42.2	45 ± 19	21.3	37 ± 20	22.1 (0.7)
45.0 ± 2.0	246 ± 48	219.9	67 ± 22	36.5	33 ± 11	19.1	36 ± 18	19.4 (0.4)
41.0 ± 2.0	214 ± 43	195.7	58 ± 17	31.0	32 ± 11	17.1	28 ± 15	17.4 (0.2)
37.5 ± 1.5	189 ± 43	168.1	51 ± 16	26.2			26 ± 14	16.0 (0.1)
34.5 ± 1.5	159 ± 36	143.2	38 ± 11	22.7			24 ± 13	17.4 (0.1)
31.5 ± 1.5	136 ± 31	115.8	36 ± 10	19.1				
28.5 ± 1.5	111 ± 26	87.4	29 ± 9	15.5				
25.5 ± 1.5	87 ± 23	60.1						

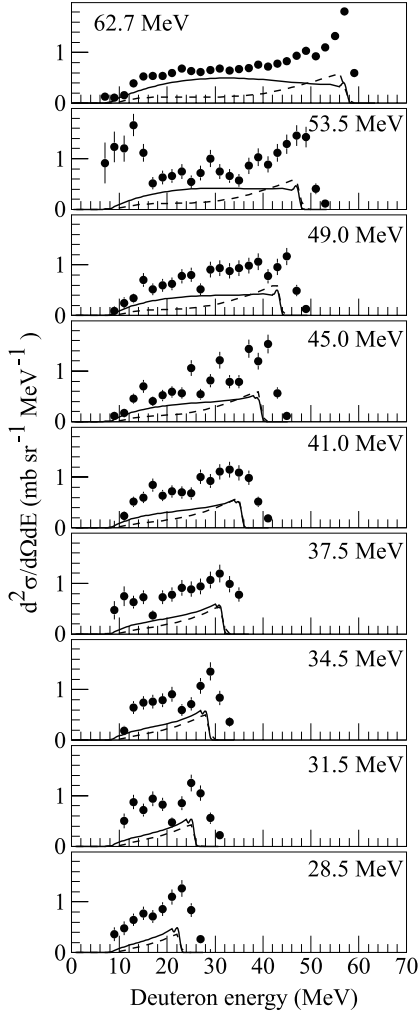


FIG. 5. Same as Fig. 4 for the deuteron emission at nine incident neutron energies.

preequilibrium part is calculated by Eq. (1), whereas the remainder of the reaction flux is distributed through the Hauser-Feshbach model. The emission rate for the ejectile k is given by

$$\omega_k(p_\pi, h_\pi, p_\nu, h_\nu, E_k) = \frac{2s_k + 1}{\pi^2 \hbar^3} \mu_k E_k \sigma_{k, \text{inv}}(E_k) \times \frac{\omega(p_\pi - Z_k, h_\pi, p_\nu - N_k, h_\nu, E_x)}{\omega(p_\pi, h_\pi, p_\nu, h_\nu, E^{\text{tot}})}, \quad (2)$$

where $\sigma_{k, \text{inv}}(E_k)$ is the inverse reaction cross section as calculated from the optical model and ω the two component particle-hole state density. For the expression of ω and the time-integrated strength S_{pre} , which determines how long the system remains in a certain exciton configuration, see Ref. [25]. The expression for S_{pre} contains the adjustable transition matrix element M^2 for each possible transition between neutron-proton exciton configurations. A two-component model, apart from being more physically sensible, allows

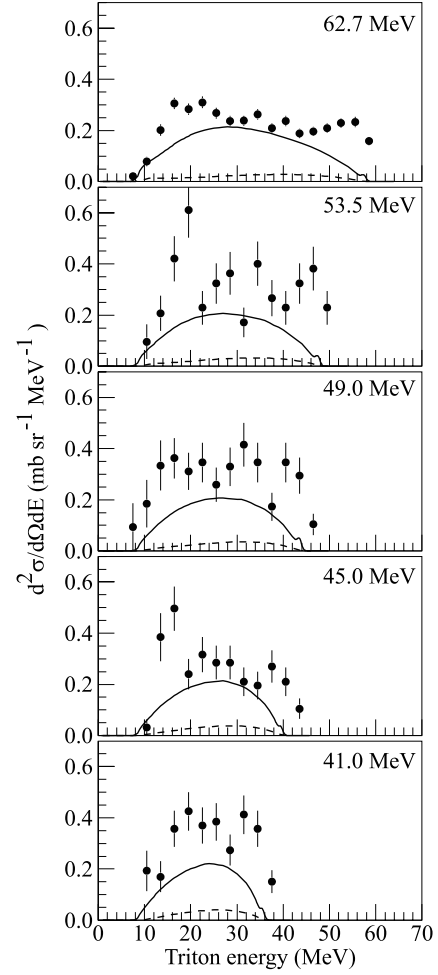


FIG. 6. Double-differential cross sections ($d^2\sigma/d\Omega dE$) for (n,tx) reactions at 20° laboratory angle, for the indicated five incident neutron energies (filled dots, in bins of 3 MeV). GNASH (dashed lines) and TALYS (continuous lines) code calculations are shown.

more flexibility in parameter adjustment. A proton-neutron ratio of 1.0 for the squared internal transition matrix elements was adopted to give the best overall agreement with experiment, i.e., $M_{\pi\pi}^2 = M_{\nu\nu}^2 = M_{\pi\nu}^2 = 2.31 \times 10^{-6} \text{ MeV}^2$, for the first $2p1h$ configuration, where π and ν stand for proton and neutron, respectively. Partial level density parameters $g_\pi = Z/15$ and $g_\nu = N/15$ were used in the equidistant spacing model for the partial level densities.

At incident energies above several tens of MeV, the residual nuclides formed after binary emission may contain so much excitation energy that the presence of further fast particles inside the nucleus becomes possible. The latter can be imagined as strongly excited particle-hole pairs resulting from the first binary interaction with the projectile. The residual system is then clearly nonequilibrated and the excited particle that is high in the continuum may, in addition to the first emitted particle, also be emitted on a short time scale. This so-called multiple preequilibrium emission forms an alternative theoretical picture of the intranuclear cascade process, whereby this time not the exact location and momentum of the particles is followed but instead the total energy

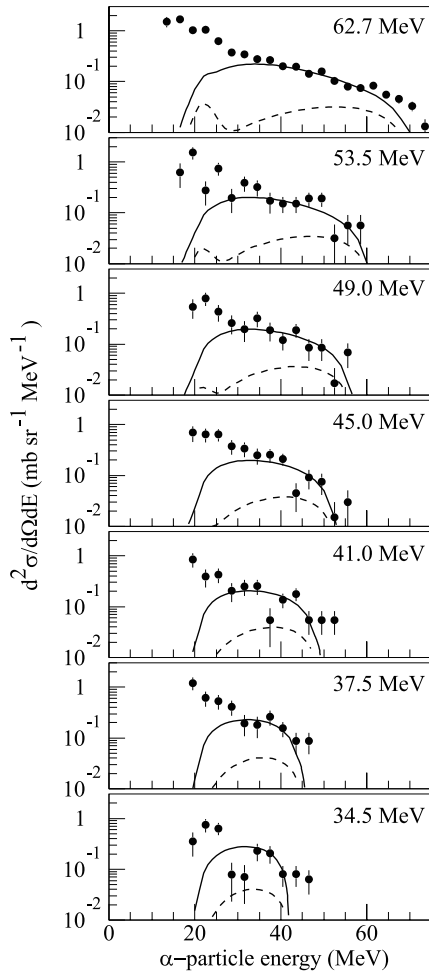


FIG. 7. Double-differential cross sections ($d^2\sigma/d\Omega dE$) for $(n, \alpha x)$ reactions at 20° laboratory angle, for seven incident neutron energies (filled dots, in bins of 3 MeV). GNASH (dashed lines) and TALYS (continuous lines) code calculations are shown.

of the system and the number of particle-hole excitations (exciton number). In actual calculations, the particle-hole configuration of the residual nucleus after emission of the ejectile, is reentered as initial condition in the calculation. When looping over all possible residual configurations, the multiple preequilibrium contribution is obtained. Multiple preequilibrium emission is followed up to arbitrary order, though for the incident energies considered in this experiment, only secondary preequilibrium emission is significant.

For preequilibrium reactions involving deuterons, tritons, helium-3 and α -particles, a contribution from the exciton model is automatically calculated both with GNASH and TALYS code using the phenomenology developed by Kalbach [27]. It is, however, well known that for nuclear reactions involving projectiles and ejectiles with different particle numbers, mechanisms such as stripping, pick-up, and knock-out play an important role and these directlike reactions are not entirely covered by the exciton model. Therefore, Kalbach [28] developed a phenomenological contribution for these mechanisms, which is included in TALYS. It is shown in the present work (see Table I) that this method gives a considerable improvement relative to GNASH calculations. The

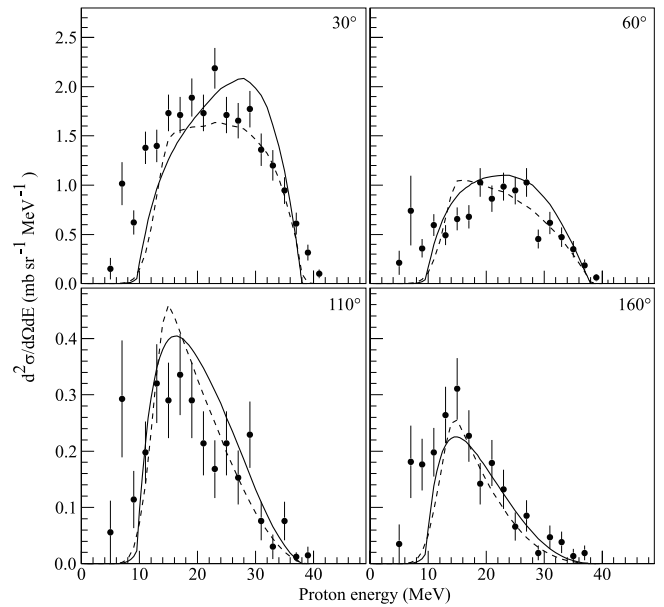


FIG. 8. Measured double-differential cross sections (filled dots in bins of 2 MeV) at four laboratory angles, for (n, px) reactions at 41.0 MeV incident neutron energy. GNASH (dashed lines) and TALYS (continuous lines) code calculations are shown.

latter results in a consistently strong underestimation of experimental data for neutron-induced reactions. Still, we wish to emphasize the highly phenomenological nature of this model. It is known that angular momentum effects play a prominent role in complex particle emission and that a more natural embedding of the pick-up mechanism in the exciton model [29] may lead to results which are not only physically

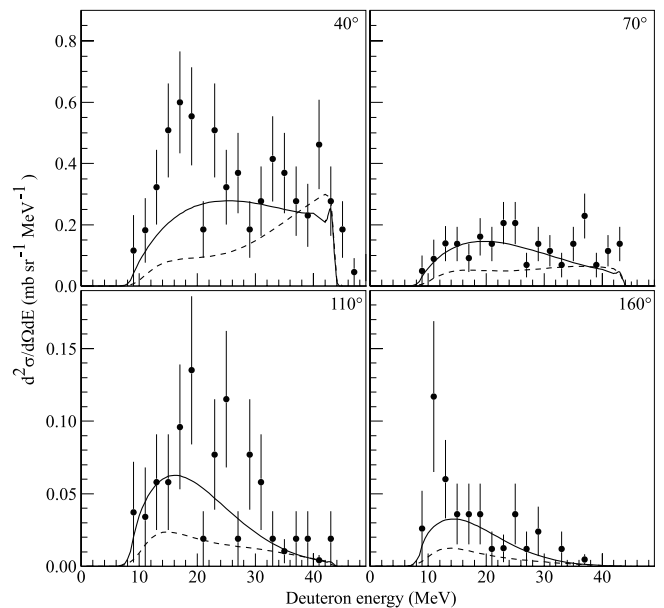


FIG. 9. Measured double-differential cross sections (filled dots in bins of 2 MeV) at four laboratory angles for (n, dx) reactions at 49.0 MeV incident neutron energy. GNASH (dashed lines) and TALYS (continuous lines) code calculations are shown.

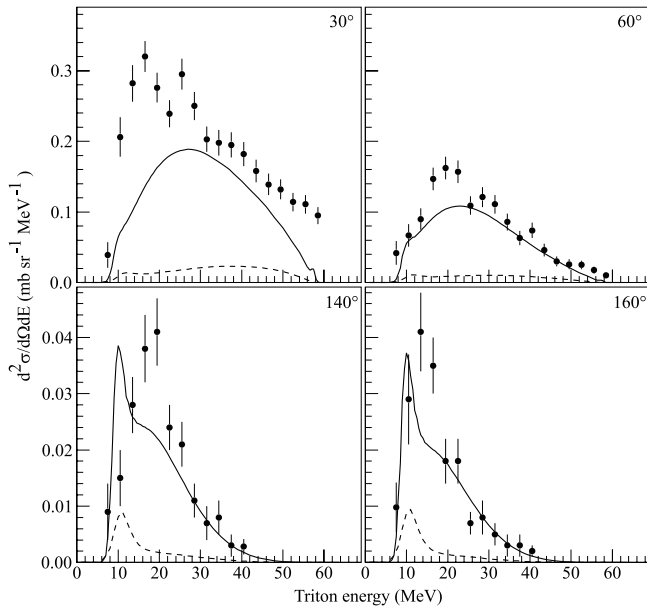


FIG. 10. Measured double-differential cross sections (filled dots in bins of 3 MeV) at four laboratory angles for (n,tx) reactions at 62.7 MeV incident neutron energy. GNASH (dashed lines) and TALYS (continuous lines) code calculations are shown.

more justified but also to a quality of fit which is, at least for α -emission, comparable to the one obtained here.

To account for the evaporation peaks in the charged-particle spectra (which are present, though small), multiple compound emission was treated with the Hauser-Feshbach model. In this scheme, all reaction chains are followed until all emission channels are closed. The compound nucleus calculations require low-lying and continuum nuclear level in-

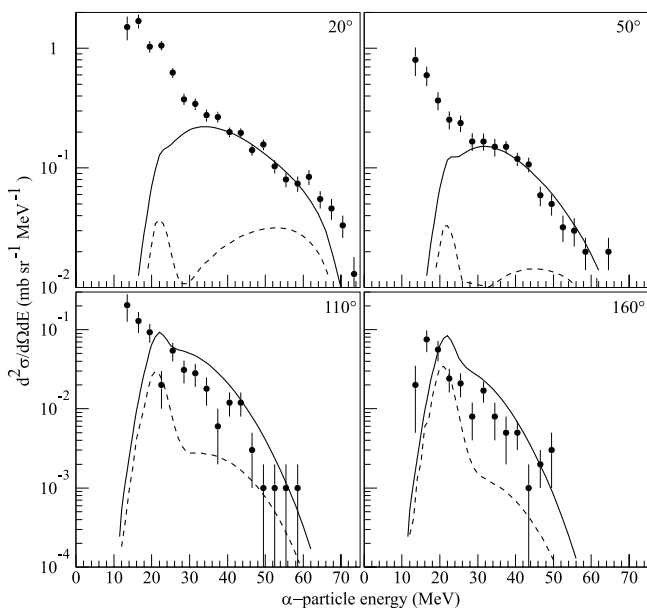


FIG. 11. Measured double-differential cross sections (filled dots in bins of 3 MeV) at four laboratory angles for $(n,\alpha x)$ reactions at 62.7 MeV incident neutron energy. GNASH (dashed lines) and TALYS (continuous lines) code calculations are shown.

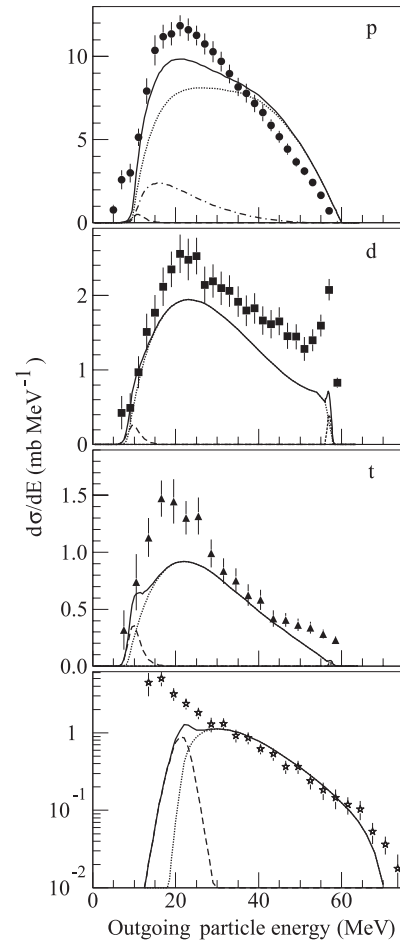


FIG. 12. Energy-differential cross sections ($d\sigma/dE$) (in 2 MeV bins for proton and deuteron and 3 MeV for triton and α -particle production) at 62.7 MeV showing contributions of primary preequilibrium (dotted lines), multiple preequilibrium (dash-dotted lines), and compound reactions (dashed lines). At high energy in the deuteron spectrum a small peak (dots) represents direct pick-up contribution.

formation for all the nuclear species that can be produced in the reaction chain. At low excitation energies, experimental nuclear level information (energies, spin, parities, and γ -ray decay branching ratios) are used [19]. For both GNASH and TALYS calculations, Ignatyuk's model [30] was adopted for the total level density to account for the damping of shell effects at high excitation energies.

It is known that semiclassical models, such as the exciton model, have always had some problems to describe angular distributions (essentially because it is based on a compound-like concept instead of a direct one). Therefore, in both the GNASH and TALYS codes the calculated energy spectra were folded with Kalbach's systematics [31] for the angular distributions. Moreover the results given by the two codes are obtained in the center-of-mass system of the recoiling nucleus plus outgoing particle. Assuming two-body kinematics, the output data as function of channel energy were transferred to data as function of laboratory outgoing particle energy.

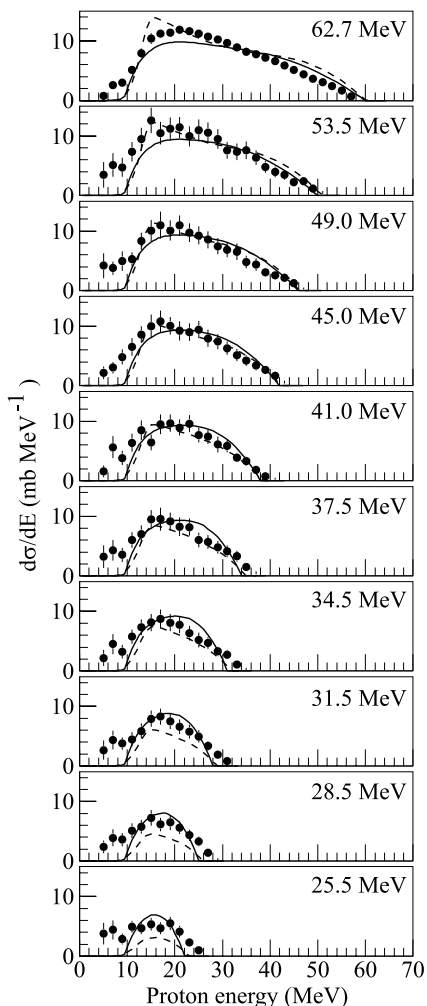


FIG. 13. Energy-differential cross sections ($d\sigma/dE$) (in bins of 2 MeV) for (n,p) reactions (filled dots). GNASH (dashed lines) and TALYS (continuous lines) code calculations are shown.

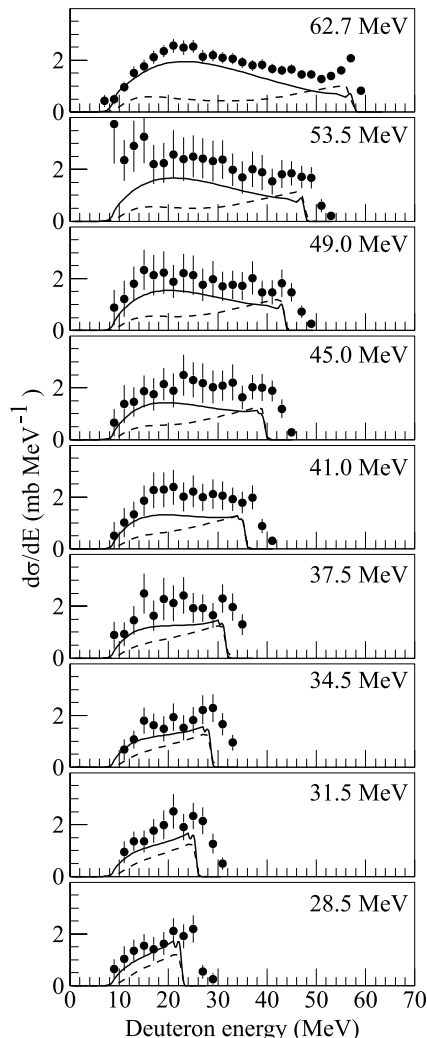


FIG. 14. Same as Fig. 13 for the deuteron case.

IV. EXPERIMENTAL RESULTS AND THEORETICAL CALCULATIONS

Double-differential cross sections ($d^2\sigma/d\Omega dE$) were measured at nine laboratory angles between 20° and 160° for proton (p), deuteron (d), triton (t), and α -particle (α) emission, at the incident neutron energies listed above. The overall relative uncertainties of the experimental points in the spectra are about 7, 12, 20, and 22% for p , d , t , and α , respectively, for 62.7 MeV data. They are mainly given by the statistics in the spectra. At lower ejectile energies, the thick target corrections [11] contribute with supplementary uncertainties. For all the other incident neutron energies (continuum) these values are between 2 and 3 times higher as a consequence of a lower incident neutron flux.

The uncertainty of the cross section absolute scale is about 7–8%, due to uncertainties in the measured reference (n,p) cross sections (5%), beam monitoring (2%), statistics in the $H(n,p)$ recoil proton peak (2–5%), solid angle corrections (1%), number of target nuclei (1%), etc.

Figures 4–7 show the double-differential cross sections (energy spectra) at 20° laboratory for p , d , t , and

α -particles (filled dots) vs the incident neutron energy. The dashed lines show calculations with the GNASH code while continuous lines show calculations with the TALYS code (a convention that is consistently respected throughout this article). Both calculations give a fair description of the proton spectra. Nevertheless, at lower incident neutron energies the TALYS calculations describe better the absolute magnitude of the experimental cross sections.

For increasingly complex ejectiles (deuterons, tritons, and α -particles), GNASH underestimates strongly the experimental data while TALYS calculations reproduce the order of magnitude and the shape of the spectra except for the low ejectile energy part (particularly in the α -particle case).

Figures 8–11 give a sampling of the angular distribution of the energy spectra at four laboratory angles for p and d at 41 and 49 MeV, respectively, and t and α -particles at 62.7 MeV incident neutron energies. The angular distributions are strongly forward peaked. Both GNASH and TALYS calculations describe well the proton spectra. For complex ejectiles, GNASH results strongly underestimate the experimental cross sections. TALYS calculations reproduce better the order of magnitude and shape of the experimental spectra. Neverthe-

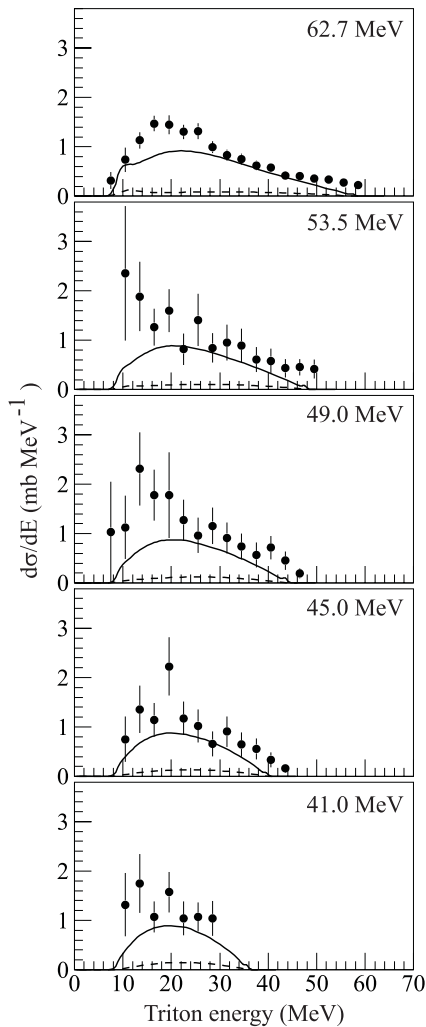


FIG. 15. Same as Fig. 14 for the (n,tx) reactions but in energy bins of 3 MeV for the outgoing particle.

less, the angular distributions are not well reproduced reflecting the fact that Kalbach's systematics [31] does not include this new experimental information, which was not available when Kalbach's systematics was done.

For each energy bin of the outgoing light charged particle spectra, the experimental angular distribution was fitted by a simple two parameter formula $a \exp(b \cos \theta)$. This allows one to extrapolate the double-differential cross sections at very forward (2.5° and 10°) and very backward (170° and 177.5°) angles, and to interpolate for the missing angles. In this way, a good covering of the laboratory angular range 0° to 180° is obtained. For each incident neutron energy, by angle integration of the above mentioned angular distributions, the corresponding energy-differential cross sections ($d\sigma/dE$) are obtained. Figure 12 presents the energy-differential spectra for p , d , t , and α -particles at 62.7 MeV incident neutron energy, compared to calculations from TALYS for different components from various reaction mechanisms. For d , t , and α -particles the multiple preequilibrium contribution is negligible. In the proton case, the primary preequilibrium contribution is the most important (a total of 301 mb). At this energy, there is a non-negligible

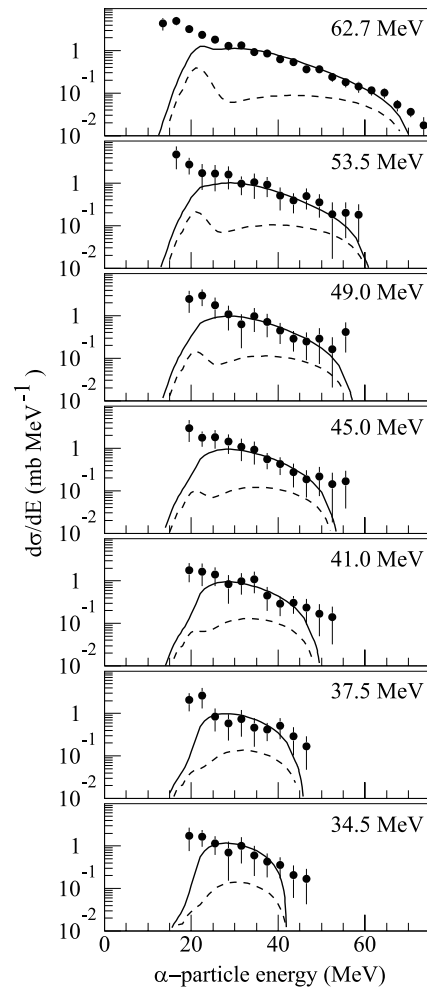


FIG. 16. Same as Fig. 15 for the $(n,\alpha x)$ reactions.

multiple preequilibrium contribution (43 mb), whereas the compound contribution (2 mb) is strongly inhibited by the Coulomb barrier. The total experimental value is 367 ± 27 mb (Table I). In the deuteron case the small peak at high energies represents direct reaction contribution (pick up).

A common feature of the GNASH and TALYS code is that charge exchange or pick-up reactions to individual states of the final nucleus are not treated individually within an explicit independent-particle approach. Rather, a smeared out contribution to these states is estimated from a continuum preequilibrium model, after which the strength is "collapsed" on the various discrete states. This explains the structure at the high-energy end of the calculated spectra for some ejectiles.

Figures 13–16 show the energy-differential cross sections for the light charged particles at all incident neutron energies. In the proton case, the two codes agree between themselves and give a good description of the spectra. Nevertheless at lower incident neutron energies TALYS agrees better with the data than GNASH calculation does. As observed above, for complex outgoing particles TALYS code gives a better description of the order of magnitude of the cross sections. At low ejectile energies, especially in the α -particle case the

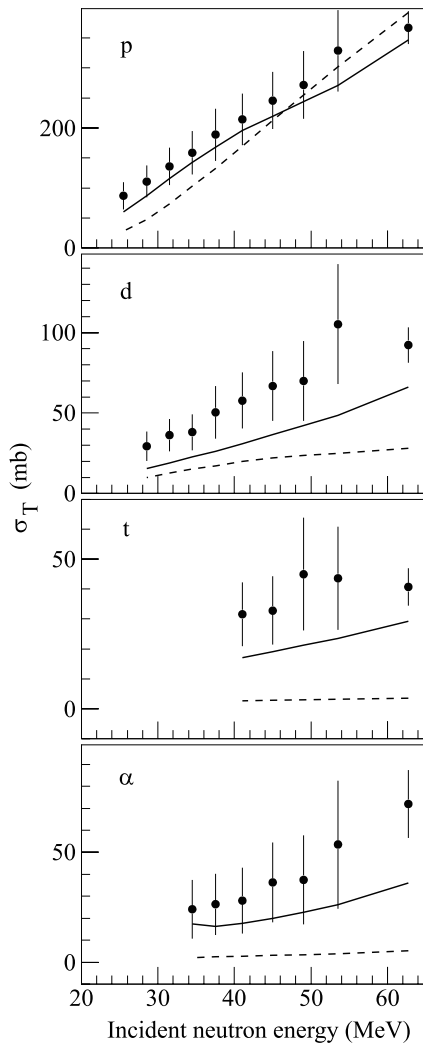


FIG. 17. Experimental total cross sections (filled dots) for (n,px) , (n,dx) , (n,tx) , and (n,ax) reactions on natural uranium vs incident neutron energy compared to values calculated by GNASH and TALYS nuclear reaction code. For numbers please see Table I. In the α -particle case, the TALYS theoretical curve includes the ${}^3\text{He}$ contribution.

calculated cross sections strongly underestimate the experimental values.

By integration of the energy-differential spectra, the total production cross sections are obtained. These values are listed in Table I. The uncertainties associated to the experimental total cross sections for triton and α -particle emission are rather high particularly for the neutron energies from the low energy continuum of the incident neutron energy spectrum. For tritons this is due to cumulated effects of (i) the rather low cross sections to be measured, therefore the low statistics accumulated and (ii) the low intensity of the neutron beam especially for energies from the low energy continuum. For the α -particles, the low statistics accumulated in the experiment is also due to the important stopping power of the target limiting the detection of α -particles to only fractions of the target thickness, even for higher energies.

The dependence of the total production cross sections for the four ejectiles vs incident neutron energy is presented in

Fig. 17 together with the theoretical values calculated by GNASH and TALYS code. For the α -particle case, the TALYS theoretical values include the ${}^3\text{He}$ contribution (included as well in the experimental values). Nevertheless, these contributions are small and within the experimental uncertainties. Compared to GNASH nuclear reaction code, the TALYS code shows a dramatic improvement especially for complex particle emission. This is due to the improved model by Kalbach [28] included in the TALYS calculation compared to the older approach [27] of GNASH.

V. CONCLUSIONS

In the present paper, a consistent experimental data set for light charged particle emission induced by fast neutrons on natural uranium is reported, covering the incident neutron energy range 25 to 65 MeV. Experimental double-differential cross sections ($d^2\sigma/d\Omega dE$), energy-differential ($d\sigma/dE$), and total production cross sections are obtained for the four types of outgoing particles at several incident neutron energies. Unfortunately there are no similar data from the neutron or proton induced reactions to compare with.

The comparison of experimental data to the theoretical calculations done with the two nuclear reaction codes (GNASH and TALYS) show clearly that the TALYS code gives a better agreement with the experimental data especially for complex ejectile (tritons and α -particle) emission. The entire difference between the predicted spectra by the two nuclear reaction codes can be attributed to the treatment of the pre-equilibrium reaction mechanism. This is due to Kalbach's improved model [28]. In the older approach [27], the accessible state density for the final nucleus only contains a contribution from the particle-hole configuration that is directly determined by the transfer reaction under consideration. In the extended mode, configurations that result from excitations of up to three particle-hole pairs are also included. Moreover, finite well-depth and surface effects are included in the particle-hole densities of the transfer model. We used this model without any adjustments, giving a description of the data that is good up to 30–40%. One expects this predictive power for complex particle emission to hold up to about 80 MeV of incident energy. At higher energies, the model needs more validation and it is expected that forthcoming measurements will bring some clarification.

From the complex particle angular distributions, it is clear that Kalbach's phenomenological description of angular distributions needs to be revised. The description of the angle-integrated spectra is quite good, whereas there are some differences between the calculations and experiment for the double-differential spectra. This is not surprising, since the present work is part of a whole new class of recent $(n,x\text{LCP})$ measurements, which were not available when Kalbach's systematics was constructed. A remaining problem is the theoretical description of the low-energy part of the α -spectrum.

Only an illustrative part of experimental results is shown in this paper. Complete data can be obtained from one of the authors (E.R.).

ACKNOWLEDGMENTS

We acknowledge support of the Institut Interuniversitaire des Sciences Nucléaires, Belgium and of the European Economic Community (Contract No. FIKW-CT-2000-00031,

HINDAS project). Dr. N. Nica thanks the Belgian French Community for partly financing his stay at the Université catholique de Louvain, Louvain-la-Neuve. Dr. S. Benck thanks the Fonds National de la Recherche Scientifique, Belgium for the financial support as a Scientific Collaborator (chargé de recherches).

-
- [1] A. Bol, P. Leleux, P. Lipnik, P. Macq, and A. Ninane, *Nucl. Instrum. Methods* **214**, 169 (1983).
- [2] C. Dupont, P. Leleux, P. Lipnik, P. Macq, and A. Ninane, *Nucl. Instrum. Methods Phys. Res. A* **256**, 169 (1983).
- [3] I. Slypen, V. Corcalciuc, A. Ninane, and J.P. Meulders, *Nucl. Instrum. Methods Phys. Res. A* **337**, 431 (1994).
- [4] D. Horn, C.G. Ball, A. Galindo-Uribarri, E. Hagberg, R.B. Walker, R. Laforest, and J. Pouliot, *Nucl. Instrum. Methods Phys. Res. A* **321**, 273 (1992).
- [5] F. Bernachi, B. Chambon, B. Cheynis, D. Drain, C. Pastor, D. Seghier, K. Zaid, A. Giorni, D. Heuer, A. Leres, C. Morand, P. Stassi, and J.B. Viano, *Nucl. Instrum. Methods Phys. Res. A* **281**, 137 (1989).
- [6] J. Alarja, A. Dauchy, A. Giorni, C. Morand, E. Pollaco, P. Stassi, R. Billery, B. Chambon, B. Cheynis, D. Drain, and C. Pastor, *Nucl. Instrum. Methods Phys. Res. A* **242**, 352 (1986).
- [7] I. Slypen, V. Corcalciuc, and J.P. Meulders, *Rom. J. Phys.* **38**, 419 (1993).
- [8] I. Slypen, Ph.D. thesis, Université Catholique de Louvain, 1995.
- [9] S. Benck, Ph.D. thesis, Université Catholique de Louvain, 1999.
- [10] S. Benck, I. Slypen, V. Corcalciuc, and J.P. Meulders, *Nucl. Phys. A* **615**, 220 (1997).
- [11] I. Slypen, V. Corcalciuc, and J.P. Meulders, *Nucl. Instrum. Methods Phys. Res. B* **88**, 275 (1994).
- [12] P.G. Young, E.D. Arthur, and M.B. Chadwick, Los Alamos National Laboratory Report No. LA-12343-MS, 1992 (unpublished); GNASH-FKK version gn9cp0, PSR-0125, program received from NEA Data Bank, 1999.
- [13] A.J. Koning and S. Hilaire (unpublished).
- [14] Data retrieved from the National Nuclear Data Center, Brookhaven National Laboratory, Upton, NY 11973-5000, Experimental Nuclear Reaction Data File EXFOR [CSISRS].
- [15] O. Bersillon, "SCAT2: A spherical optical model code," Report No. CEA-N-2227, 1981 (unpublished).
- [16] Final report to the European Commission, Report No. EUR 19794 (unpublished).
- [17] J. Bojowald, H. Machner, H. Nann, W. Oelert, M. Rogge, and P. Turek, *Phys. Rev. C* **38**, 1153 (1988).
- [18] C.M. Perey and F.G. Perey, *At. Data Nucl. Data Tables* **17**, 1 (1976).
- [19] Data retrieved from RIPL, Reference Input Parameter Library for theoretical calculations of nuclear reactions, URL <http://IAEAND.IAEA.OR.AT/ripl/>
- [20] A.J. Koning and J.P. Delaroche, *Nucl. Phys. A* **713**, 231 (2003).
- [21] S. Watanabe, *Nucl. Phys.* **8**, 484 (1958).
- [22] H. Gruppelaar, P. Nagel, and P.E. Hodgson, *Riv. Nuovo Cimento* **9**, 1 (1986).
- [23] E. Gadioli and P.E. Hodgson, *Pre-equilibrium Nuclear Reactions* (Oxford University Press, Oxford, 1992).
- [24] C. Kalbach, *Phys. Rev. C* **32**, 1157 (1985).
- [25] C. Kalbach, *Phys. Rev. C* **33**, 818 (1986).
- [26] A.J. Koning, S. Hilaire, M. Duivestijn, and J.P. Delaroche (unpublished).
- [27] C. Kalbach, *Z. Phys. A* **283**, 401 (1977).
- [28] C. Kalbach, Users manual for PRECO-2000: "Exciton model pre-equilibrium code with direct reactions," Duke University, 2001, retrieved from URL www.nndc.bnl.gov/nndcscr/model-codes/preco-2000/
- [29] J. Bisplinghoff, *Phys. Rev. C* **50**, 1611 (1994).
- [30] A.V. Ignatyuk, G.N. Smirenkin, and A.S. Tishin, *Sov. J. Nucl. Phys.* **21**, 255 (1975).
- [31] C. Kalbach, *Phys. Rev. C* **37**, 2350 (1988).